



Chinese Pharmaceutical Association
Institute of Materia Medica, Chinese Academy of Medical Sciences

Acta Pharmaceutica Sinica B

www.elsevier.com/locate/apsb
www.sciencedirect.com



ORIGINAL ARTICLE

ACAT1 deficiency in myeloid cells promotes glioblastoma progression by enhancing the accumulation of myeloid-derived suppressor cells



Mingjin Wang, Weida Wang, Shen You, Zhenyan Hou, Ming Ji, Nina Xue, Tingting Du, Xiaoguang Chen*, Jing Jin*

Department of Pharmacology, State Key Laboratory of Bioactive Substances and Functions of Natural Medicines, Institute of Materia Medica, Chinese Academy of Medical Sciences and Peking Union Medical College, Beijing 100050, China

Received 30 May 2023; received in revised form 9 July 2023; accepted 9 August 2023

KEY WORDS

Glioblastoma;
Myeloid cells;
Myeloid-derived suppressor cells;
Acetyl-CoA acetyltransferase 1;
CXCL1;
Tumor microenvironment;
Lipid metabolism;
Macrophages

Abstract Glioblastoma (GBM) is a highly aggressive and lethal brain tumor with an immunosuppressive tumor microenvironment (TME). In this environment, myeloid cells, such as myeloid-derived suppressor cells (MDSCs), play a pivotal role in suppressing antitumor immunity. Lipid metabolism is closely related to the function of myeloid cells. Here, our study reports that acetyl-CoA acetyltransferase 1 (ACAT1), the key enzyme of fatty acid oxidation (FAO) and ketogenesis, is significantly downregulated in the MDSCs infiltrated in GBM patients. To investigate the effects of ACAT1 on myeloid cells, we generated mice with myeloid-specific (*LyzM-cre*) depletion of ACAT1. The results show that these mice exhibited a remarkable accumulation of MDSCs and increased tumor progression both ectopically and orthotopically. The mechanism behind this effect is elevated secretion of C–X–C motif ligand 1 (CXCL1) of macrophages ($M\phi$). Overall, our findings demonstrate that ACAT1 could serve as a promising drug target for GBM by regulating the function of MDSCs in the TME.

© 2023 Chinese Pharmaceutical Association and Institute of Materia Medica, Chinese Academy of Medical Sciences. Production and hosting by Elsevier B.V. This is an open access article under the CC BY-NC-ND license (<http://creativecommons.org/licenses/by-nc-nd/4.0/>).

*Corresponding authors. Tel./fax: +86 10 63165207.

E-mail addresses: chxg@imm.ac.cn (Xiaoguang Chen), rebeccagold@imm.ac.cn (Jin Jing).

Peer review under the responsibility of Chinese Pharmaceutical Association and Institute of Materia Medica, Chinese Academy of Medical Sciences.

<https://doi.org/10.1016/j.apsb.2023.09.005>

2211-3835 © 2023 Chinese Pharmaceutical Association and Institute of Materia Medica, Chinese Academy of Medical Sciences. Production and hosting by Elsevier B.V. This is an open access article under the CC BY-NC-ND license (<http://creativecommons.org/licenses/by-nc-nd/4.0/>).

1. Introduction

Glioma is a prevalent form of cancer in the central nervous system that arises from transformed neural stem or glial progenitor cells^{1,2}. According to the World Health Organization, gliomas are classified into four groups based on their histopathological characteristics. Low-grade gliomas, including grades I and II, are typically well-differentiated and slow-growing tumors. On the other hand, high-grade gliomas, including grades III and IV, are less differentiated or anaplastic, and they tend to infiltrate brain parenchyma more strongly. Among them, grade IV glioma, also known as glioblastoma (GBM), is the most malignant and aggressive form of brain cancer in adults. Despite advances in surgical ablation, radiotherapy, and high-dose chemotherapy^{3–5}, the median survival for patients is only 14–16 months, with a 5-year survival rate of less than 3%. According to reports, the tumor microenvironment (TME) characterized by immune suppression is a crucial factor contributing to the progression of GBM and drug resistance. This immunosuppressive TME comprises diverse myeloid cells, such as bone marrow-derived macrophages (BMDM), microglia, myeloid-derived suppressor cells (MDSCs), dendritic cells (DC), and neutrophils^{1,6,7}. Among these myeloid cells, MDSCs are considered the most potent in suppressing the immune response and strongly inhibiting cancer-specific cytotoxic T-cell function⁸. In mouse models, depletion of MDSCs has been shown to significantly enhance anti-tumor immunity^{8–10} and improve the effectiveness of checkpoint inhibitors like anti-PD1 antibodies¹¹. Therefore, the manipulation of MDSCs has emerged as a promising target for the development of anti-cancer therapies.

Lipid metabolism is a crucial biological process, which encompasses various metabolic pathways, such as fatty acid metabolism, cholesterol metabolism, ketone body metabolism, and acetate metabolism among others. Recent studies have increasingly explored dysregulated lipid metabolism in GBM^{12,13}. Lipid rewiring has emerged as a characteristic feature of GBM, wherein lipids serve as vital sources of cellular maintenance and energy^{13,14}. In conjunction with the Warburg effect, lipid metabolism has been recognized as essential for GBM progression¹⁵. Furthermore, this metabolic system plays a critical role in regulating the function of MDSCs. Previous studies have indicated that polyunsaturated fatty acids (PUFA) can promote the expansion of hematopoietic progenitor cells into MDSCs *in vitro*, leading to larger tumors in mice with PUFA-enriched diets¹⁶. The infiltration of MDSCs in tumor tissue with elevated reactive oxygen species (ROS) production driven by the signal transducer and activator of transcription 3 (STAT3) axis exacerbates the tumor's growth^{17,18}. Additionally, increased lipid absorption mediated by CD36 and CD204 enhances the immunosuppressive function of MDSCs^{19,20}. Hematopoietic progenitors were unable to differentiate in the absence of FAO, which phenomenon could be rescued by acetate supplementation²¹. One important enzyme in lipid metabolism is ACAT1, which is located in mitochondria and catalyzes the reversible reaction that converts acetoacetyl-CoA to two molecules of acetyl-CoA^{22,23}. This enzyme is involved in the last step of FAO and the first step of ketogenesis, and it also has acetyltransferase activity. Recent studies have shown that ACAT1 has a regulatory effect on various biological processes, such as inhibiting the activity of mutant isocitrate dehydrogenase 2 (mIDH2) R140Q by acetylating its K413 in acute myeloid leukemia cells²⁴ and maintaining the aerobic glycolysis of cancer cells by acting as the upstream acetyltransferase of pyruvate dehydrogenase

alpha^{23,25}. However, the role of ACAT1 in MDSCs remains understudied despite its importance as a key metabolic regulatory protein.

In our study, we first investigated the relationship between ACAT1 expression and myeloid cell ratio in the tumor of GBM patients. To achieve this, we analyzed single-cell RNA-seq (scRNA-seq) data from biopsies of human primary glioma surgical specimens available in the gene expression omnibus (GEO) database. Our analysis revealed that ACAT1 expression was inversely proportional to the myeloid cell ratio in the tumor. To elucidate the role of myeloid cells' ACAT1 in GBM progression, we generated *Acat1* gene conditional knockout (*Acat1*^{fl^{ox}/fl^{ox}} LyzM-cre^{+/+}, *Acat1*-CKO) mice. Our findings indicate that ACAT1 plays a crucial role in the regulation of differentiation and biological activity of MDSCs. Depletion of ACAT1 in myeloid cells led to the accumulation of MDSCs and the formation of an immunosuppressive TME in mice bearing GBM. This, in turn, promoted the growth of ectopic and orthotopic brain glioblastoma xenografts G422. Importantly, our results suggest that this phenomenon might be closely related to the elevated level of CXCL1 after ACAT1 depletion. Thus, targeting ACAT1 may represent a promising approach for the treatment of GBM by regulating MDSCs in the TME.

2. Materials and methods

2.1. scRNA-seq data analysis

For analyzing scRNA-seq data, the scRNA-seq data matrix of glioblastoma patient tumor tissues (GSM2758474, GSM2758477, GSM4483741, GSM4483751, GSM4483755, GSM4483758, GSM5705583, GSM4119533) was downloaded from GEO database (<https://www.ncbi.nlm.nih.gov/gds/>). The samples selected were obtained from untreated GBM (WHO Grade IV) patients using the 10 × genomics single-cell transcriptome sequencing technology. The patient cohort consisted of individuals aged between 45 and 70, without any gender restrictions. To ensure accuracy in the analysis results, we selected samples with a reasonably similar range of cell numbers (total cell range: 1000–5000) that encompassed the detection of myeloid cells. Additionally, we specifically excluded IDH-mutant samples to eliminate potential metabolic interference. Seurat (v4.0.0) package was used for quality control processing of data. Cells with >200 retained genes, >1000 UMI, <0.7 log₁₀GenesPerUMI, <10% mitochondrial UMI, and <5% red blood cell genes were treated as high-quality cells, then DoubletFinder software was used for double cell removal to perform downstream analysis. The FindVariableGenes function in the Seurat package is used to screen highly variable genes (HVGs), and the expression profiles of HVGs are used to conduct the mutual nearest neighbors (MNN) dimension reduction analysis. The batch effect of single-cell expression profile data was corrected, and the results were visualized in two-dimensional space using uniform manifold approximation and projection (UMAP) nonlinear dimensionality reduction. Based on the marker expression of myeloid cells²⁶, we identified the location of myeloid cells in the UMAP plot and calculated the proportion of myeloid cells in each sample.

2.2. Animal experiments

Two lox sites were inserted into the first and eighth introns using a CRISPR/Cas9-based genome-editing technology to create *Acat1*-

CKO mice in both cases. Small guide RNA (sgRNA) was synthesized using a donor vector and transfected *In vitro*. To create F0 generation mice, C57BL/6J mouse zygotes were microinjected with Cas9, sgRNA, and donor. To create conditional knockout mice, we bred *Acat1*-CKO animals that had been floxed with *LyzM*-cre mice purchased from Cyagen Biosciences. The *LyzM*-cre mice have been fully backcrossed to C57BL/6J mice from SPF Biotechnology (over more than 10 generations). *LyzM*-cre animals lacking *Acat1*^{fllox/fllox} have been utilized as wildtype controls for *Acat1*^{fllox/fllox} *LyzM*-cre mice. All of the mice were bred and cared for in a pathogen-free environment. Animal operations were carried out in accordance with the Peking Union Medical College's Guidelines for Animal Experiments after gaining approval from the Institutional Animal Care and Use Committee of the Institute of Materia Medica, Chinese Academy of Medical Sciences & Peking Union Medical College. Both male and female mice were utilized in the tests. Animals were randomly allocated to experimental groups. Genotypes were determined by PCR using primers specific for *LyzM*-cre (Reverse primer: 5'-CTT GGG CTG CCA GAA TTT CTC-3', Forward primer: 5'-TTA CAG TCG GCC AGG CTG AC-3' for wildtype and 5'-CCC AGA AAT GCC AGA TTA CG-3' for mutant) and specific for *Acat1* flox site (Reverse primer: 5'-TCC ACT TGG TCA CAG GTC ACA G-3', Forward primer: 5'-TCC TAG AGC CTG AGA ACC AGT CAG-3').

2.3. Mouse G422 glioma cell xenograft model

Mouse G422 glioma cells (5×10^5 cells) in 0.2 mL of saline were injected subcutaneously into the right flank of *Acat1*-CKO and *LyzM*-cre mice ($n = 6$ per group) to establish ectopic glioma. The tumor volume was measured twice weekly from the day after the implant of the tumor. The weight of the tumors was measured and studied after the 14th day of the mice's exposure to the tumor. For the intracranial tumor research, mice were anesthetized with 50 mg/kg sodium pentobarbital before receiving 2×10^5 G422 cells in 5 μ L PBS under the direction of a stereotaxis device. Skull holes were pierced to the right striatum at mediolateral 2 mm, anteroposterior -0.8 mm, dorsoventral 3.6 mm bregma. The weight and wellness of the animals were assessed twice a week. Small animal MRI scanner (Pharma Scan 70/16 US, Bruker) were used to examine the anatomical images of the intracranial tumors after 14 days of Intracranial injection.

2.4. Immunohistochemistry (IHC)

Slides holding tumor or spleen tissue were heated for 15 min at 65 °C before being rehydrated with xylene, 100%, 95%, 85%, and 75% ethanol. Then, the citrate target retrieval solution, pH 6.0, was used for the antigen retrieval technique in the microwave. Slides were blocked for 10 min in Hydrogen Peroxide Block (ZSGB-BIO) and blocked in 5% BSA-PBS buffer for 30 min, then incubated with primary antibody at a 1:100 dilution in 1% BSA-PBS at 4 °C. Antibodies used were Arg1 (Cell Signaling Technology), Gr-1 (BioLegend), Ki67 (Cell Signaling Technology), and CXCL1 (Proteintech). Slides were washed in PBS and then incubated with secondary antibody (ZSGB-BIO) for 20 min. After washing, DAB chromogen (ZSGB-BIO) was prepared according to the manufacturer's instructions and added to slides while observing the staining under a microscope. ddH₂O was used to quench the reaction, and dehydrated slides from 85% ethanol to xylene. The mounting medium was used to mount the slides.

2.5. Western blot

The tumor tissue and MDSCs isolated from the spleens using a mouse MDSC isolation kit (Miltenyi Biotec) were lysed in RIPA buffer (Solarbio) supplemented with protease inhibitor cocktail (TargetMol) and phosphatase inhibitor cocktail (Solarbio). Protein extracts were clarified and concentrations were measured with the BCA Protein Assay Kit (Lablead). Western blot procedure was performed as previously described²⁷. Briefly, cell lysates were then subjected to 10% SDS-polyacrylamide gel electrophoresis and transferred to polyvinylidene fluoride membranes (Millipore). The membranes were probed overnight at 4 °C with antibodies specific for iNOS (Cell Signaling Technology), Arg1 (Cell Signaling Technology), CD3e (Santa Cruz Biotechnology), Gr-1 (BioLegend), ACAT1 (Cell Signaling Technology), β -actin (ZSGB-BIO) followed by incubation for 1 h at room temperature with secondary antibodies conjugated with peroxidase. Membrane-bound immune complexes were detected with the high-sig ECL Detection Reagent (Tanon) on Tanon-5200 Chemiluminescent Imaging System (Tanon).

2.6. Flow cytometry

To obtain tumor-infiltrating cells, tumors were digested in RPMI 1640 (Gibco) supplemented with 1 mg/mL collagenase type IV (Sigma-Aldrich) and 0.1 mg/mL DNaseI (Sigma-Aldrich) for 60 min at 37 °C. The single-cell samples of the spleen were harvested by mechanical disintegration with 100 μ m cell strainers (Biosharp). All red blood cells of the tumor, spleen, and blood samples need be lysed using red blood cell lysis buffer (Salorbio). Block of Fc-mediated reactions by purified anti-CD16/CD32 antibody (clone 93, BioLegend) for 10 min on ice before immunostaining, then stained with indicated antibodies for 30 min on ice. Antibodies for MDSC and DC: CD45 (PerCP/Cyanine5.5, clone 30-F11, BioLegend), CD11b (APC, clone M1/70, BioLegend), F4/80 (APC/Cyanine7, clone BM8, BioLegend), Ly6G (PE, clone 1A8, BioLegend), Ly6C (PE/Cyanine7, clone HK1.4, BioLegend), CD11c (FITC, clone N418, BioLegend). Antibodies for M ϕ : CD11b (APC, clone M1/70, BioLegend), F4/80 (APC/Cyanine7, clone BM8, BioLegend), MHCII (PerCP/Cyanine5.5, clone M5/14.15.2, BioLegend), CD206 (PE, Clone C068C2, BioLegend). Antibodies for T cells: CD3 (APC/Cyanine7, clone 17A2, BioLegend), CD4 (PerCP/Cyanine5.5, clone GK1.5, BioLegend), CD8 (PE/Cyanine7, clone 53-6.7, BioLegend), FOXP3 (PE, clone 150D, BioLegend), IFN- γ (APC, clone XMG1.2, BioLegend). For IFN- γ and FOXP3 staining, samples were stimulated by 1640 medium containing 50 ng/mL PMA, 500 ng/mL ionomycin, and $1 \times$ BFA for 4 h, then cells were fixed and permeabilized with eBioscience FOXP3/Transcription Factor Staining Buffer Set (Invitrogen) and stained with IFN- γ and FOXP3 after CD3/CD4/CD8 staining. Flow cytometry was performed using the standard protocol on the BD FACSVerse analyzer (Becton Dickinson), and data were analyzed with the FlowJo software (FlowJo LLC).

To examine the major histocompatibility complex II (MHCII) expression of BMDM, the BMDM was isolated and cultured from *LyzM*-cre and *Acat1*-CKO mice. Cells were stained with CD11b (APC/Cyanine7, clone 17A2, BioLegend), F4/80 (APC/Cyanine7, clone 17A2, BioLegend), MHCII (APC/Cyanine7, clone 17A2, BioLegend). Then the MHCII positive cell proportion was examined by flow cytometry.

2.7. BM-MDSC culture and treatment

LyzM-cre or *Acat1*-CKO mice's bone marrow was used to generate bone marrow-derived MDSCs (BM-MDSCs). After red blood cell lysis, bone marrow cells at a density of 5×10^6 cells/mL were cultured in the complete RPMI medium containing GM-CSF (100 ng/mL, PeproTech) and IL-6 (100 ng/mL, PeproTech) for 4 days. And 1 and 10 nmol/L of CXCL1 (PeproTech) were added on Day 0. To examine the effect of M ϕ -secreted cytokine on MDSC differentiation, the culture supernatants of normal BMDM and *Acat1* knockout (*Acat1*^{-/-}) BMDM were collected and added to complete 1640 medium containing GM-CSF (100 ng/ml) and IL-6 (100 ng/mL) in a certain proportion, the C-X-C motif chemokine receptor 2 (CXCR2) inhibitor SB225002 (MCE) was added to selected cultures to a final concentration of 2 μ mol/L to eliminate the effect of CXCL1 on the generation of MDSCs. The generation of MDSCs stained with CD11b (APC, clone M1/70, BioLegend), Gr1 (PE, clone RB6-8C5, BioLegend) was tested by BD FACSVerser analyzer.

2.8. Cell viability assay

Cell viability was accessed by CellTiter-Glo (CTG, Promega) assay according to the manufacturer's protocol. Briefly, GL261 mouse glioma cells were seeded in 96-well culture plates at a density of 4000 cells/well in 100 μ L medium. Subsequently, 100 μ L of MDSCs (5×10^4 cells) isolated from the spleen using a Mouse MDSC Isolation Kit (Miltenyi Biotec) were added to co-culture with GL261 cells. The co-cultures were incubated at 37 °C, 5% CO₂ for 96 h. After the incubation, 100 μ L of CTG reagent was added to each well and shaken for 1 min. The plates were then kept at room temperature for 10 min to stabilize the luminescence signal. Luminescence was measured using a microplate reader (SYNERGY H1, BIO-TEK).

2.9. Suppression of T cell proliferation assay

To evaluate the T cell suppressive effect of MDSC on T cell proliferation, a T cell suppression assay was conducted as previously described²⁸. T cells were isolated from splenocytes of 8- to 12-week-old mice using a Pan T Cell Isolation Kit II (Miltenyi Biotec). The isolated T cells were stained with 1 μ mol/L carboxyfluorescein succinimidyl ester (CFSE, BioLegend) for 5 min at 37 °C and washed with ice-cold PBS twice. To activate T cells, plate-bound anti-mouse CD3 (1 μ g/mL, Biolegend) and soluble anti-mouse CD28 (5 μ g/mL, Biolegend) antibodies were used. The activated T cells were co-cultured at a 1:1 ratio with *in vitro*-generated mouse MDSCs (1×10^5 cells) derived from bone marrow cells. The co-cultures were established in 96-well round bottom plates and incubated for 72 h. Following co-culture, the cells were stained with anti-CD8a antibody (PerCP/Cyanine5.5, clone 53-6.7, BioLegend), T-cell proliferation was measured by the dilution of CFSE fluorescence using flow cytometry (on gated CD8⁺ T cells). The divided ratio was determined and analyzed with the FlowJo software.

2.10. MDSC depletion with anti-Gr1 mAbs

After tumor cell injection in the right supra-scapular region of mice, 100 μ L anti-Gr1 (200 μ g, Clone RB6-8C5, BioLegend) mAbs were injected intraperitoneally every 72 h. MDSC-depletion

efficiency after tumor inoculation was validated by flow cytometry.

2.11. BMDM isolation and culture

For mouse BMDM preparation²⁹, cells of the femur and tibia bones of the aforementioned mouse strains were flushed. Erythrocytes were removed using red blood cell lysis buffer (Salorbio) after centrifuging for 5 min at $450 \times g$. The remaining cells were seeded in plates, and the complete RPMI 1640 medium with 50 ng/mL recombinant mouse M-CSF (PeproTech) was used as the incubation medium for 7 days to form nonactivated cells (M0).

2.12. Cytokines and chemokines measurement

The levels of CXCL1, TGF- β 1, IL-18, IL-23, MDC, IL-10, IL-12p:70, IL-6, TNF- α , G-CSF, TARC, IL-12p:40, IL-1 β , IFN- γ , IL-5, TNF- α , IL-2, IL-4, IL-9, IL-17A, IL-17F, IL-22, IL-13 in tumor tissue and supernatant of resting M ϕ , LPS-stimulated M ϕ were determined with the LEGENDplex Mouse Macrophage/Microglia Panels (Biolegend) and LEGENDplex Mouse Th Chemokine Panel (Biolegend) per the manufacturer's instructions. Tissue lysate was screwed in PBS and the protein level was normalized to the same level. Bead fluorescence was measured using the BD FACSVerser flow cytometer and analyzed in the LEGENDplex data analysis software (Biolegend). CXCL1 levels in plasma samples were measured by mouse CXCL1/KC enzyme-linked immunosorbent assay (ELISA) Kit (absin). The procedure was strictly by the kit instructions and the required indicators were measured in a microplate reader (Synergy H1, BIO-TEK).

2.13. Gene set enrichment analysis (GSEA)

Extraction of total RNA of resting BMDM by TRIzol Reagent (Invitrogen) from above-mentioned mice. The transcriptome sequencing and analysis were conducted by OE Biotec. Trimmomatic was used to process raw data (raw readings). To get the clean reads, the ploy-N-containing and low-quality reads were eliminated. Then the clean reads were mapped to the reference genome using hisat2. FPKM value of each gene was calculated using cufflinks, and the read counts of each gene were obtained by htseq-count. Gene set enrichment analysis was performed using the gene set enrichment analysis tool (GSEA, Broad Institute).

2.14. BMDM phagocytosis-capability determination

To measure M ϕ phagocytosis, BMDM cells were allowed to ingest 1% (v/v) Fluorescein-conjugated Zymosan Particles (BioVision) for 1 h at 37 °C or 0.1% (v/v) 2 μ m FluoSphere Carboxylate-Modified Microspheres (Invitrogen) for 20 min at 37 °C in a CO₂ incubator. Most of the extra particles were removed with three washes in PBS. To remove any bound particles from the cell surface and the plate, the cells were next taken to a 1 h trypsin/EDTA treatment at 37 °C. Finally, the cells were fixed with 2% paraformaldehyde and examined using flow cytometry at 488 nm, and the data were analyzed with the FlowJo software.

2.15. Seahorse XFe24 analyzer

Four mitochondrial parameters (basal respiration, maximal respiration, proton leak, and ATP production) were evaluated using the

Seahorse XFe24 Analyzer (Agilent Technologies). Briefly, 50,000 BMDMs were seeded per well in special 24-well plates and cultured overnight. Cells were changed to incubate in modified DMEM (containing 1 mmol/L sodium pyruvate, 10 mmol/L glucose, and 2 mmol/L glutamine) as the culture medium for 1 h at 37 °C without CO₂. Then, to measure the four different mitochondrial characteristics, the Seahorse XF Cell Mito Stress Test Assay was carried out using 1 mol/L oligomycin, 2 mol/L carbonyl cyanide-4-(trifluoromethoxy)phenylhydrazone, 0.5 mol/L antimycin, and rotenone. Data were analyzed with Wave2.6.0.31 software (Agilent Technologies).

2.16. Tumor challenge and SB225005 treatment experiments

SB225002 was prepared as a solution containing 1% DMSO, 20% polyethylene glycol 400, 5% tween 80, and 74% ddH₂O. Following the establishment of G422 ectopic glioma in LyzM-cre and *Acat1*-CKO mice, SB225002 was administered at a dose of 10 mg/kg *via* intraperitoneal injection (i.p.) daily. All mice were randomly assigned to different treatment cohorts. On Day 14, mice were humanely euthanized for further analysis.

2.17. Statistical analysis

All data are shown as mean \pm standard error of mean. Several independent replications are presented in the corresponding Figure legends. Two-tailed *t*-tests were used to evaluate statistical differences. The RNA-seq (FPKM format) data of integrin subunit alpha M (ITGAM)[ENSG00000169896.16] in normal tissue ($n = 1157$) and tumor ($n = 489$) downloaded from The Cancer Genome Atlas (TCGA) database and the Genotype-Tissue Expression (GTEx) database was calculated using the Wilcoxon rank sum test. All statistical analysis was calculated by GraphPad Prism7 software. Unless specifically indicated, statistical significance was considered as a two-sided *P* value < 0.05.

3. Result

3.1. ACAT1 expression of myeloid cells is lower in high-myeloid-infiltration human glioma

RNA-seq data analysis of glioma patients (GBMLGG) from TCGA database and normal tissue from GTEx database revealed that the expression of the myeloid marker ITGAM was significantly higher in tumor tissue compared to normal tissue ($P = 2.17E-63$), which indicates a marked increase in myeloid cell infiltration in tumor tissue (Fig. 1A). 8 scRNA-seq data of specimens of untreated human GBM was chosen randomly from GEO datasets (GSE148842³⁰, GSE103224³¹, GSE138794³², GSE189650³³) and analyzed. The resulting data showed that the single cells were arranged in two dimensions based on the similarity of their highly variable gene expression profiles by the dimensionality reduction technique UMAP, resulting in 10 distinct cell clusters (Fig. 1B). Two different clusters (#4, #9) corresponded to myeloid cells, which expressed multiple known myeloid markers²⁶, including C1QA, HLA-DRA, CD14, AIF1, TYROBP, and CD163 (Fig. 1C). The ratio of myeloid cells in these samples was shown in Fig. 1D. To determine whether lipid metabolism was involved in the function of myeloid cells and the development of GBM, Pearson's correlation analysis was utilized to analyze the correlations between the average expression of

genes related to fatty acid metabolism (PATHWAY: has01212 of KEGG) in the myeloid cluster and the ratio of myeloid cells in GBM. Among the top 10 genes involved in fatty acid metabolism related to the ratio of myeloid cells, ACAT1, an enzyme that catalyzes the final step of mitochondrial FAO and exhibits a significant expression in myeloid cells, was identified (Fig. 1E, Supporting Information Table S1), thereby capturing our attention. As shown in Fig. 1F, the average expression of ACAT1 in the identified myeloid cells was negatively correlated with the proportion of tumor-infiltrating myeloid cells.

3.2. ACAT1 conditional knockout in mice accelerates G422 tumor growth in vivo

To evaluate whether ACAT1 is related to the function of myeloid cells and tumor development, we established *Acat1*-CKO mice (Fig. 2A–C). We then observed the growth of G422 glioma cell xenograft transplanted tumors in both LyzM-cre and *Acat1*-CKO mice. As shown in Fig. 2D and E, the tumor growth of the ectopic glioma was significantly increased in *Acat1*-CKO mice compared to LyzM-cre mice, with the average weight of *Acat1*-CKO tumors being three times heavier than LyzM-cre tumors. Accordingly, the expression of Ki67, a cell proliferation antigen in cancer^{34,35}, was much higher in the tumors of *Acat1*-CKO mice than in LyzM-cre mice (Fig. 2F, $P = 0.0031$), which was correlated with the difference in tumor proliferation curve between the two groups. Encouraged by the xenograft model results, we established an orthotopic transplantation model of G422. As shown in Fig. 2G, on the 14th day, the average tumor volume in the striatum of LyzM-cre mice was 287.3 mm³, while *Acat1*-CKO tumors grew to 967.6 mm³ ($P = 0.0229$). Moreover, the expression of Ki67 was remarkably higher in *Acat1*-CKO mice compared to LyzM-cre mice (Fig. 2H, $P = 0.0015$). Thus, depletion of ACAT1 in myeloid cells significantly accelerates tumor proliferation, suggesting that myeloid cells' ACAT1 may play a potential role in the immune microenvironment.

3.3. Robust immunosuppressive TME is formed in tumors of *Acat1*-CKO mice

To determine whether the depletion of ACAT1 in myeloid cells affected the TME, we examined leukocytes in both tumor tissue (Fig. 3A) and blood (Supporting Information Fig. S1A–S1D) using flow cytometry, and the gating strategy for flow cytometry data was shown in Supporting Information Fig. S2. Fig. 3A reveals that while the percentage of immune cells (CD45⁺) in *Acat1*-CKO mice tumors significantly decreased relative to LyzM-cre mice ($P = 0.00057$), there was a marked increase in the proportion of myeloid cells (CD45⁺/CD11b⁺, $P = 0.0014$), g-MDSC (CD45⁺/CD11b⁺/Ly6c⁻/Ly6g⁺, $P = 3.8E-6$), m-MDSC (CD45⁺/CD11b⁺/Ly6c⁺/Ly6g⁻, $P = 0.0038$) and M ϕ (CD45⁺/CD11b⁺/F480⁺/Ly6c⁻/Ly6g⁻, $P = 2.6E-5$) in *Acat1*-CKO mice tumors. In the absence of ACAT1, there is a significant reduction in the proportion of M1 in M ϕ populations (Supporting Information Fig. S3A, $P = 1.47E-6$), while it does not affect the proportion of M ϕ differentiation into M2-like M ϕ (Fig. S3B). The proportion of DCs, which play a crucial role in anti-tumor processes, remains unaffected in the tumor of LyzM-cre and *Acat1*-CKO mice (Fig. S3C). As reported, iNOS and Arg1 could directly inhibit the function and proliferation of T cells^{36,37}, especially their anti-tumor activities^{38–40}. The immunosuppressive factors such as Arg1 and TGF- β were

upregulated significantly, and expression of iNOS was also increased slightly, consistent with the elevation of immunosuppressive cells (Fig. 3B and C). Furthermore, the anti-tumor cytokine IFN- γ was significantly reduced (Fig. 3C). As illustrated by Fig. 3D, compared with LyzM-cre mice, the ratio of immunosuppressive T cells (CD45⁺/CD3⁺/CD4⁺/FoxP3⁺) to CD4⁺T cells increased ($P = 0.025$), while the number of CD3⁺T cells in *Acat1*-CKO mice was significantly reduced ($P = 0.00002$), and there was a decreased proportion of cytotoxic lymphocytes (CTLs, CD45⁺/CD3⁺/CD8⁺/IFN γ ⁺) ($P = 0.016$). Similar results were found in G422 orthotopic transplanted mice (Supporting Information Fig. S4A–S4D). These findings indicated an immunosuppressive TME caused by the depletion of ACAT1 in myeloid cells.

Furthermore, the number of MDSCs in the spleen, which is the primary storage organ for MDSCs⁴¹, was analyzed in G422 xenotransplant mice. Fig. 3E illustrates a significant increase in Gr1⁺ MDSCs in the spleen due to the suppression of ACAT1 in myeloid cells, and the spleen index, depicted in Fig. S4E ($P = 0.00026$), also showed a marked increase. Moreover, MDSCs isolated from the spleen of *Acat1*-CKO mice demonstrated significantly higher expression of Arg1 and iNOS compared to LyzM-cre mice (Fig. 3F). The cellular viability of mouse glioma cell line GL261 was evaluated by co-culturing it

with MDSCs for a duration of 72 h. The results reveal a significant enhancement in tumor cell proliferation when co-cultured with MDSCs lacking ACAT1 (Fig. 3G). In the representative experiment shown in Fig. 3H, the addition of ACAT1-deficient BM-MDSCs led to the suppression of CD8⁺T cell proliferation, as evidenced by an increased percentage of cells in the parental generation and a parallel decrease in the percentage of proliferating cells. These findings highlight the stronger immunosuppressive properties of ACAT1-deficient MDSCs and suggest a critical involvement of MDSCs in the accelerated tumor growth observed in *Acat1*-CKO mice.

3.4. Tumor growth promotion in *Acat1*-CKO mice is due to MDSC

There is strong evidence suggesting that MDSCs among myeloid cells have a significant role in establishing the impressive tumor immune microenvironment, leading to resistance to cancer immunotherapy^{1,6,42}. To investigate whether MDSCs were the principal tumor proliferative factor due to ACAT1 depletion in myeloid cells, purified anti-mouse Ly-6G/Ly-6C (Gr-1) Antibody was utilized to eliminate MDSCs in both LyzM-cre and *Acat1*-CKO mice bearing G422 cells (Fig. 4A). Remarkably, tumor growth differences between the two groups disappeared

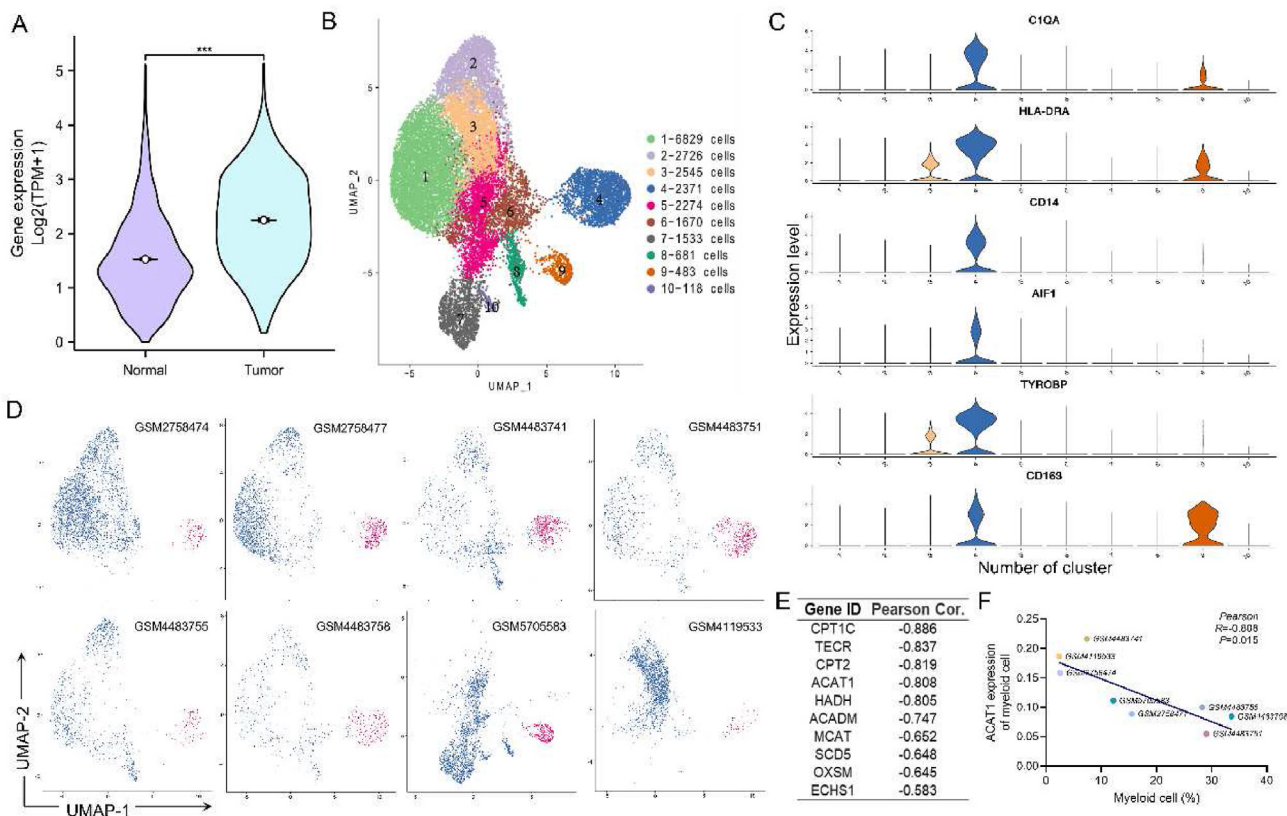


Figure 1 ACAT1 expression of myeloid cells is lower in high-myeloid-infiltration human glioma. (A) Violin plot of the comparison of ITGAM expression in normal tissue ($n = 1157$) and tumor ($n = 489$) with the Wilcoxon rank sum test. $***P = 2.17E-63$. (B) UMAP plots and cell clustering analysis. Ten different clusters were identified. (C) Violin plot showing expression of known myeloid markers in each cell cluster, #4 and #9 were identified as myeloid cell clusters. (D) UMAP plots and proportion analysis of myeloid cells (red) and other cells (blue) of human glioma surgical specimens. (E) List of the top 10 genes involved in fatty acid metabolism related to the myeloid cells ratio. Pearson coefficient is indicated. (F) Linear regression analysis of ACAT1 expression in the identified myeloid cells and myeloid cells ratio of tumor tissue used Pearson's correlation coefficients. $R = -0.808$.

after MDSC ablation (Fig. 4B and C), and spleen weight was comparable in both groups (Fig. 4D). Simultaneously, the representative IHC image of spleen tissue showed a significant decrease in the number of myeloid cells, while the lymphocyte ratio had rebounded in the spleen (Fig. 4D). Furthermore, unlike the G422 xenograft tumor model without injected anti-Gr1 antibody, there were no substantial changes among different immune cells (such as total leukocytes and subtypes of MDSCs) in the tumor (Fig. 4E). However, the differences between CD11b⁺ cells and Mφs ($P = 0.0014$) in both groups still existed (Fig. 4E and F).

After the elimination of MDSCs, differences in the number of total T cells and Treg cells in the tumor disappeared, and the CD8⁺T cells' cytotoxic capability was recovered (Fig. 4G). The immunosuppressive status of tumors in *Acat1*-CKO mice was

decreased significantly, as shown by the detection of Arg1 through IHC (Fig. 4H). These results suggest that depletion of ACAT1 in myeloid cells induced an immunosuppressive TME that was mainly attributed to the increase in MDSC of the tumor tissue, though ACAT1 knockout can affect a variety of myeloid cells, such as Mφs and DCs.

3.5. CXCL1, as a key factor, promotes MDSCs accumulation after ACAT1 depletion

The generation of MDSCs is primarily caused by the multi-effects of inflammatory cytokines and chemokines on bone marrow-derived immature myeloid cells (IMCs)^{43–45}. Therefore, the LEGENDplex multiplex assays were used to detect the related cytokines and chemokines in the tumor tissue and blood

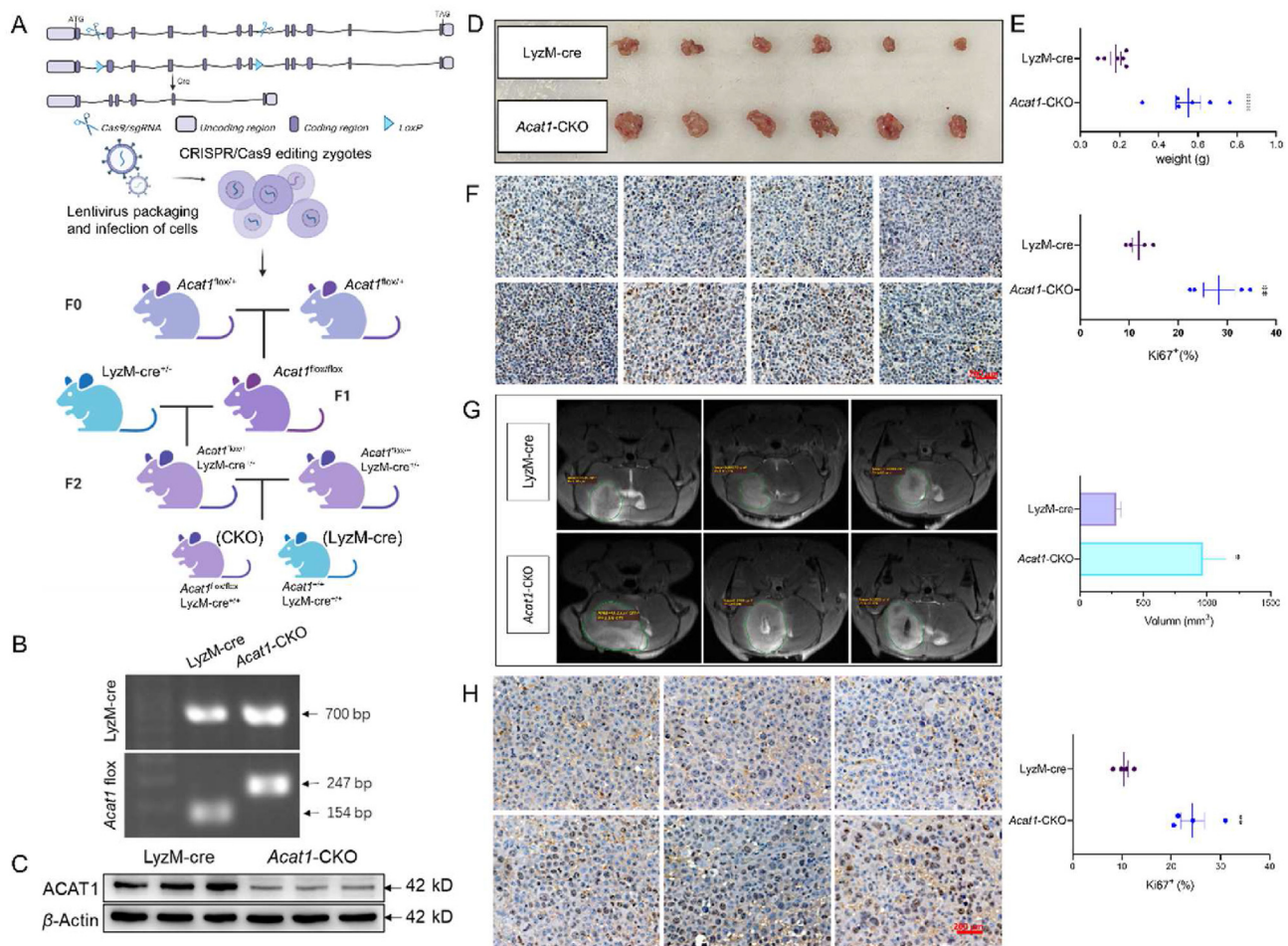


Figure 2 Effect of myeloid *Acat1*-deletion in mice glioblastoma G422 growth. (A) A scheme for CRISPR/Cas9-mediated genome editing of the *Acat1* gene locus. LoxP sites (blue arrowheads) were introduced flanking exons 2 and 7 to generate the *Acat1*^{flox/flox} construct (top, left). To obtain myeloid cells inactivation of ACAT1, *Acat1*^{flox/flox} mice were crossed with *LyzM-cre*^{+/+} and *Acat1-CKO* mice. (B) Genotyping of *LyzM-cre*^{+/+} and *Acat1-CKO* mice. (C) Analysis of ACAT1 and β -actin in bone marrow derived macrophage from 8-week-old *LyzM-cre*^{+/+} ($n = 3$) and *Acat1-CKO* ($n = 3$) mice. (D, E) Tumor image (D) and tumor weight (E) in *LyzM-cre* and *Acat1-CKO* mice that were injected subcutaneously with G422 ($n = 6$ mice per group), mice were sacrificed after the 14th day. *** $P = 0.0003$. (F) Images (left) of Ki67 IHC of ectopic glioma sections (4 images per group). Scale bars, 200 μ m. Analysis of Ki67⁺ ratio (right) in tumor section ($n = 4$) with software ImageJ. ** $P = 0.0031$. (G) Tumor image scanned with small animal MRI scanner (left) and tumor volume (right) in *LyzM-cre* and *Acat1-CKO* mice that were orthotopic transplantation with G422 ($n = 3$ mice per group, * $P = 0.0229$). Tumor volume (mm^3) = Maximum area (mm^2) \times Piles number with tumor $\times 0.5$. (H) Images (left) of Ki67 IHC of intracranial glioma sections (3 images per group). Scale bars, 200 μ m. Analysis of Ki67⁺ ratio (right) in tumor section ($n = 4$) with software ImageJ. ** $P = 0.0015$.

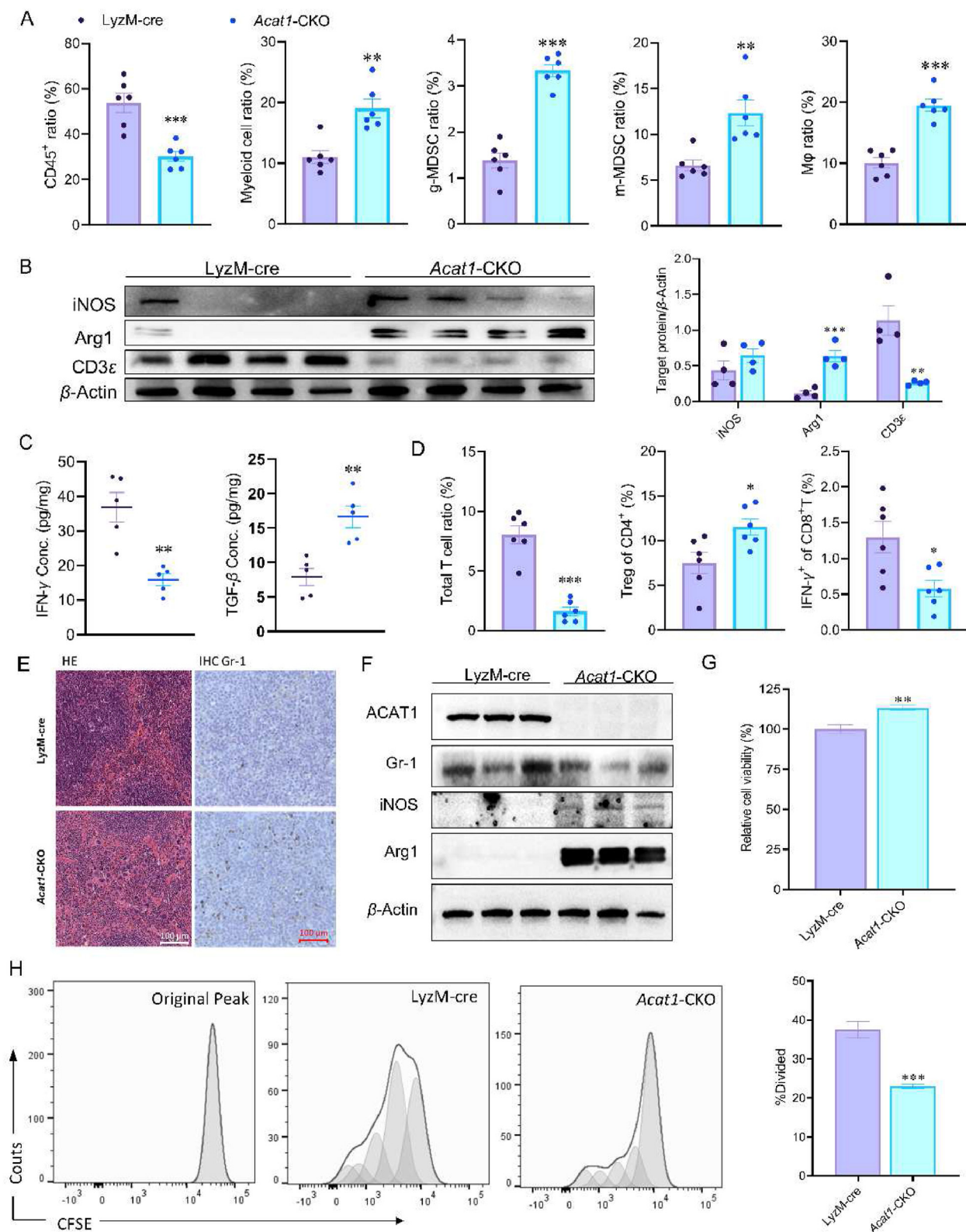


Figure 3 Robust immunosuppressive TME is formed in tumors of *Acat1*-CKO mice. (A) Percentage of the indicated leukocyte subsets in ectopic G422 tumors of LyzM-cre ($n = 6$) and *Acat1*-CKO ($n = 6$) mice at 14 days post-tumor cells inoculation, as determined by flow cytometry. (B) iNOS, Arg1, CD3ε and β-actin expression in tumor tissue of LyzM-cre ($n = 4$) and *Acat1*-CKO ($n = 4$) mice as determined by Western blot. Integrated optical density (IOD, right) was analyzed by ImageJ software. $**P = 0.0056$, $***P = 0.00093$. (C) Concentration of IFN-γ and TGF-β in tumors of LyzM-cre ($n = 5$) and *Acat1*-CKO ($n = 5$) mice tested with the LEGENDplex Mouse Macrophage/Microglia Panels and Th Chemokine Panel. $**P = 0.0018$, $**P = 0.0026$. (D) Percentage of total T cells in the tumor tissue, Treg (FoxP3⁺) in CD4⁺,

(Supporting Information Fig. S5A and S5B). As illustrated in Fig. 5A, the level of CXCL1 was significantly increased in the tumor of *Acat1*-CKO mice, which was consistent with the IHC results of tumor sections (Fig. 5B). CXCL1, being a chemokine, mainly exerts its effects on bone marrow-derived IMCs through the blood, inducing chemotaxis and accumulation of MDSCs in blood and organs^{45,46}. Thus, ELISA was used to measure the serum concentration of CXCL1. As shown in Fig. 5C, the serum CXCL1 was significantly elevated in both tumor-free mice and G422 xenografts of *Acat1*-CKO mice. The upregulated level of serum CXCL1 in tumor-free mice inspired us to consider the possibility that some stromal cells contributed to the observed differences between *Acat1*-CKO and *LyzM*-cre groups. Corresponding to the rising CXCL1 concentration in *Acat1*-CKO mice without tumor burden, the proportion of g-MDSC (CD11b⁺ Ly6G⁺) and m-MDSC (CD11b⁺ Ly6C⁺) in the blood of *Acat1*-CKO tumor-free mice was increased, and the proportion of T cells was significantly decreased (Fig. 5D). This phenomenon is consistent with the increased CXCL1 level in the serum of tumor-free mice.

MDSCs are generated from bone marrow and can migrate to immune organs or be recruited to the TME, contributing to cancer development⁴⁷. To investigate if CXCL1 promotes MDSCs accumulation, bone marrow cells derived from *LyzM*-cre and *Acat1*-CKO mice were cultured in a complete RPMI medium containing IL-6 and GM-CSF for 4 days and stimulated with CXCL1 at doses ranging from 100 pmol/L to 10 nmol/L. Then, Flow cytometry was used to identify MDSCs through staining with CD11b and Gr1 antibodies. As demonstrated in Fig. 5E, bone marrow cells stimulated with CXCL1 differentiated into MDSCs in a dose-dependent manner. This phenomenon was more prominent in *Acat1*-CKO mice compared to *LyzM*-cre mice. Therefore, CXCL1, as the main chemokine and promotor of MDSC, is responsible for the MDSC accumulation in *Acat1*-CKO mice, and bone marrow cells from *Acat1*-CKO mice were more likely to differentiate into MDSCs.

3.6. *Mφ secretes more CXCL1 after ACAT1 knockout*

CXCL1 is primarily produced by Mφs and exerts its effects through CXCR2 on the cell surface^{46,48}. The transcriptome analysis of BMDM from *LyzM*-cre and *Acat1*-CKO mice was conducted. GSEA analysis revealed a significant disruption in the cytokine secretion of BMDM after ACAT1 knockout (Fig. 6A). ACAT1 knockout resulted in a significant increase in the expression of CXCL1 in Mφ (Fig. 6A), and this phenomenon was further validated in *ex vivo* BMDM of M0 and M1 status (Fig. 6B). To confirm whether the production of CXCL1 by ACAT1-depleted Mφs secreted more CXCL1 led to the accumulation of MDSCs, bone marrow cells were cultured with different ratios of culture supernatant from BMDMs of *LyzM*-cre and *Acat1*-CKO mice (Fig. 6C). As illustrated in Fig. 6D, bone marrow cells cultured with the supernatant from ACAT1-knockout BMDMs inclined

further towards the differentiation of MDSCs in a ratio-dependent manner. This effect was reversed by the inhibition of CXCR2 using the SB225002 inhibitor, which blocked CXCL1's signaling transduction (Fig. 6D). To demonstrate that MDSCs accumulation is dependent on CXCL1 production following ACAT1 depletion, SB225002 was administered at 10 mg/kg by i.p. injection every day. As shown in Fig. 6E and F, blockade of the receptor for CXCL1 by SB225002 resulted in a deceleration of tumor growth in *Acat1*-CKO mice, accompanied by elimination in the disparity of tumor weight between *LyzM*-cre and CKO groups. Furthermore, SB225002 effectively decreased the levels of MDSCs within *Acat1*-CKO mouse tumors, thereby eliminating the discrepancy in MDSC proportions between *LyzM*-cre and *Acat1*-CKO groups (Fig. 6G). This finding implies that CXCL1 is a crucial mediator produced by BMDMs post-ACAT1 deletion, playing a role of utmost importance in the induction of MDSCs and accelerated tumor growth of the *Acat1*-CKO group.

The transcriptome data revealed that the oxidative phosphorylation level of Mφs was disrupted following ACAT1 deletion (Supporting Information Fig. S6A). Recent research has shown that pro-inflammatory Mφ has lower levels of mitochondrial oxidative phosphorylation (OXPHOS)⁴⁹. Seahorse data from BMDMs revealed that basal respiration, maximal respiration, ATP production, and spare respiratory capacity significantly decreased after ACAT1 deletion (Fig. S6B and S6C). These findings imply that Mφs tend towards a pro-inflammatory phenotype and have a limited capability for OXPHOS. The phagocytic ability of Mφs, vital for their anti-tumor role^{7,50}, was assessed using fluorescein-conjugated zymosan particles and carboxylate-modified microspheres. The results indicated that the phagocytic capacity of BMDMs was significantly reduced upon ACAT1 deletion (Fig. S6D and S6E). MHCII, responsible for the presentation of antigen to T helpers and the development of the immune response⁵¹, was significantly downregulated in *Acat1*-knockout BMDMs (Fig. S6F). Taken together, the results suggest that *Acat1*-deficient Mφs are unable to effectively exert anti-tumor immune responses but secrete more CXCL1, leading to the promotion of MDSC accumulation.

4. Discussion

GBM, the most aggressive and malignant primary brain tumor in adults, exhibits high resistance to immunotherapy due to its unique immune microenvironment^{52,53}. Myeloid cells are the most predominant contributors of immune components making up the GBM microenvironment^{52,53}. MDSCs, originating from aberrant myelopoiesis induced by a large array of pathologic conditions including cancer and chronic infection, are crucial components of the suppressive network that promotes tumor progression and contributes to therapy resistance^{54,55}. The frequency of MDSCs within the tumor and in the systemic circulation is associated with glioma progression and therapeutic interventions targeting MDSCs have shown promising effects in GBM⁵⁴. Consistent with

IFN- γ ⁺ in CD8⁺ of *LyzM*-cre ($n = 6$) and *Acat1*-CKO ($n = 6$) mice 14 days post-tumor cells inoculation determined by flow cytometry. (E) Representative images of hematoxylin and eosin (H&E) or Gr1-stained splenic sections of *LyzM*-cre and *Acat1*-CKO mice with ectopic G422 tumor. Scale bar, 100 μ m. (F) Expression of ACAT1, Gr-1, iNOS, Arg1, and β -actin of MDSCs isolated from the spleens of *LyzM*-cre ($n = 3$) and *Acat1*-CKO mice ($n = 3$) with a Mouse MDSC Isolation Kit analyzed by Western blot. (G) Cell viability of GL261 cells co-cultured with MDSCs isolated from the spleen of *LyzM*-cre ($n = 4$) and *Acat1*-CKO ($n = 4$) mice was estimated by using CTG assay. ** $P = 0.0044$. (H) Proliferation proportion of CD8⁺ T cells co-cultured with ACAT1-deficient BM-MDSCs ($n = 4$), compared with T cells co-cultured by BM-MDSCs from *LyzM*-cre mice ($n = 4$). *** $P = 0.00055$.

the clinical observations, our research revealed the accumulation of MDSCs in *Acat1*-CKO mice, which facilitated glioma growth. Notably, this phenomenon was abrogated upon MDSC depletion with an anti-Gr1 antibody (Fig. 4). In the TME, MDSCs can rapidly differentiate into immunosuppressive M ϕ , DC⁴⁷. In the research, we observed an increased abundance of M ϕ in tumors of ACAT1-deficient mice (Fig. 3A). The quantity of MDSCs in the tumor is positively correlated with the expression of iNOS and Arg1. iNOS produces large amounts of nitric oxide, which can suppress the activity of antigen-presenting cells by affecting the expression of MHCII molecules and inducing T-cell apoptosis. Arg1 produced by MDSCs depletes essential nutrients for T cells, such as L-arginine and L-cysteine, leading to downregulation of the ζ -chain in the T cell receptor (TCR) complex and inhibition of

antigen-driven T cell proliferation⁵⁶. Moreover, MDSCs can upregulate the expression of immunosuppressive factors like IL-10 and TGF- β , promoting the activation and expansion of Treg cells⁵⁴. In our study, we found a high infiltration of MDSCs in the transplanted tumors of ACAT1-deficient mice, accompanied by elevated expression of iNOS, Arg1, TGF- β , and T cell exhaustion (Fig. 3B–D). And MDSCs isolated from the spleen of ACAT1-deficient mice also exhibited high levels of iNOS and Arg1 secretion (Fig. 3F), inhibited CD8⁺T cell proliferation (Fig. 3H). Furthermore, MDSCs can directly promote tumor development by influencing angiogenesis, enhancing tumor invasiveness and metastasis, and augmenting the stemness of tumor cells. Co-culture experiments of MDSCs with GL261 cells demonstrated that ACAT1-deficient MDSCs can directly promote tumor cell

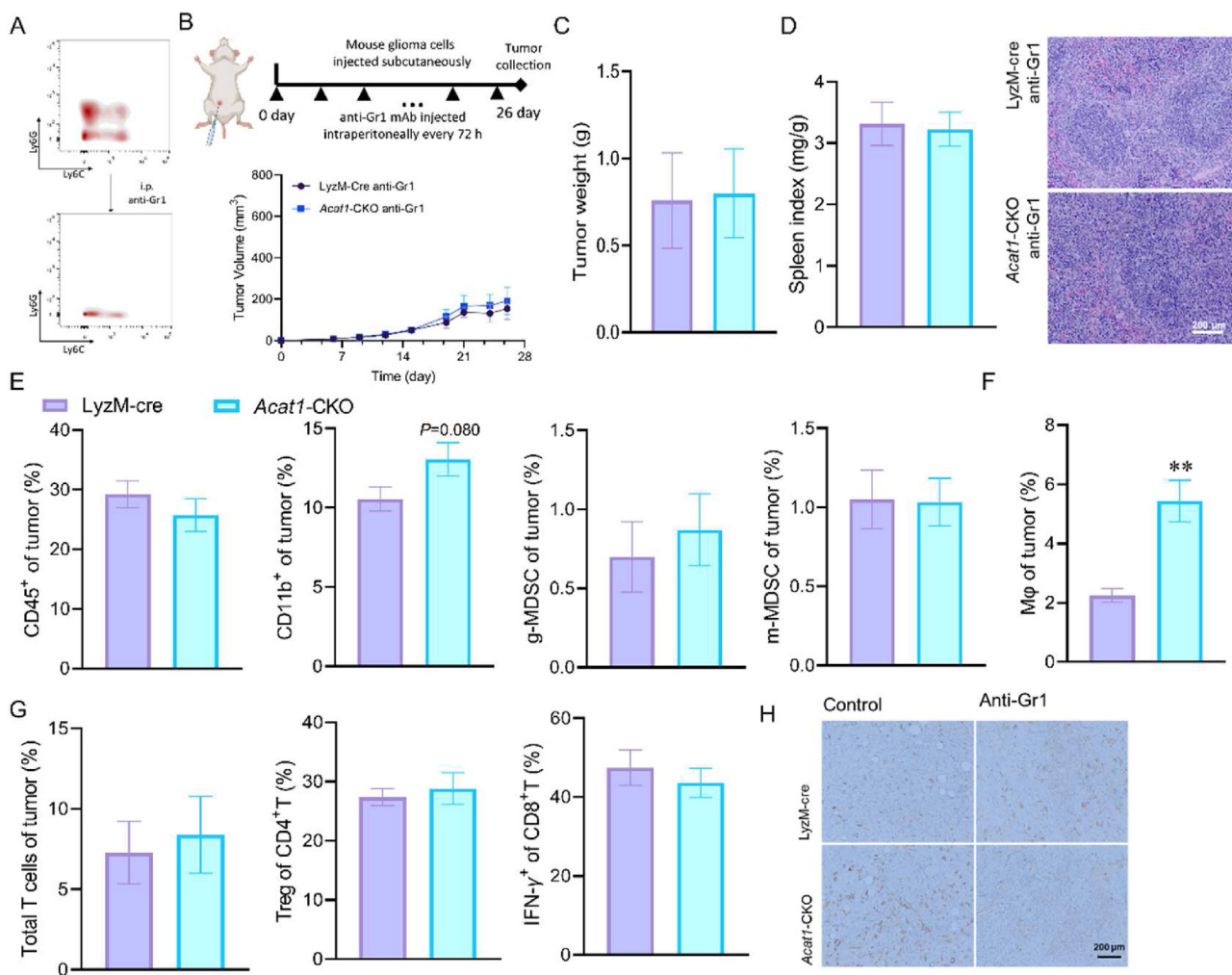


Figure 4 Tumor growth promotion in *Acat1*-CKO mice is due to MDSC. (A) Purified anti-mouse Ly-6G/Ly-6C (Gr-1) antibody could eliminate MDSCs of mice bearing G422 cells. (B) 100 μ L anti-Gr1 (200 μ g) mAbs were injected intraperitoneally every 72 h following glioma cells injected (upper). Tumor growth volume (lower) change in LyzM-cre ($n = 4$) and *Acat1*-CKO ($n = 4$) mice injected with ectopic G422 and anti-Gr-1, tumors were collected after the 26th day. (C) Tumor weight of LyzM-cre ($n = 4$) and *Acat1*-CKO ($n = 4$) mice injected with G422 and anti-Gr-1. (D) Spleen index and representative images of H&E splenic section of indicated groups. Scale bar, 200 μ m. (E) Percentage of the indicated leukocyte subsets in ectopic G422 tumors of LyzM-cre ($n = 6$) and *Acat1*-CKO ($n = 6$) mice injected anti-Gr1 mAb at 26 days post-tumor cells inoculation, as determined by flow cytometry. (F) M ϕ (CD45⁺/CD11b⁺/F480⁺) ratio in tumor ($n = 6$) of indicated groups. ** $P = 0.0014$. (G) Percentage of total T cells in the tumor, Treg (FoxP3⁺) in CD4⁺, IFN- γ ⁺ in CD8⁺ of LyzM-cre ($n = 6$) and *Acat1*-CKO ($n = 6$) mice injected anti-Gr1 mAb at 26 days post-tumor cells inoculation determined by flow cytometry. (H) Representative images of Arg1-stained splenic sections (four images per mouse) of LyzM-cre and *Acat1*-CKO mice with ectopic G422 tumor. Scale bar, 200 μ m.

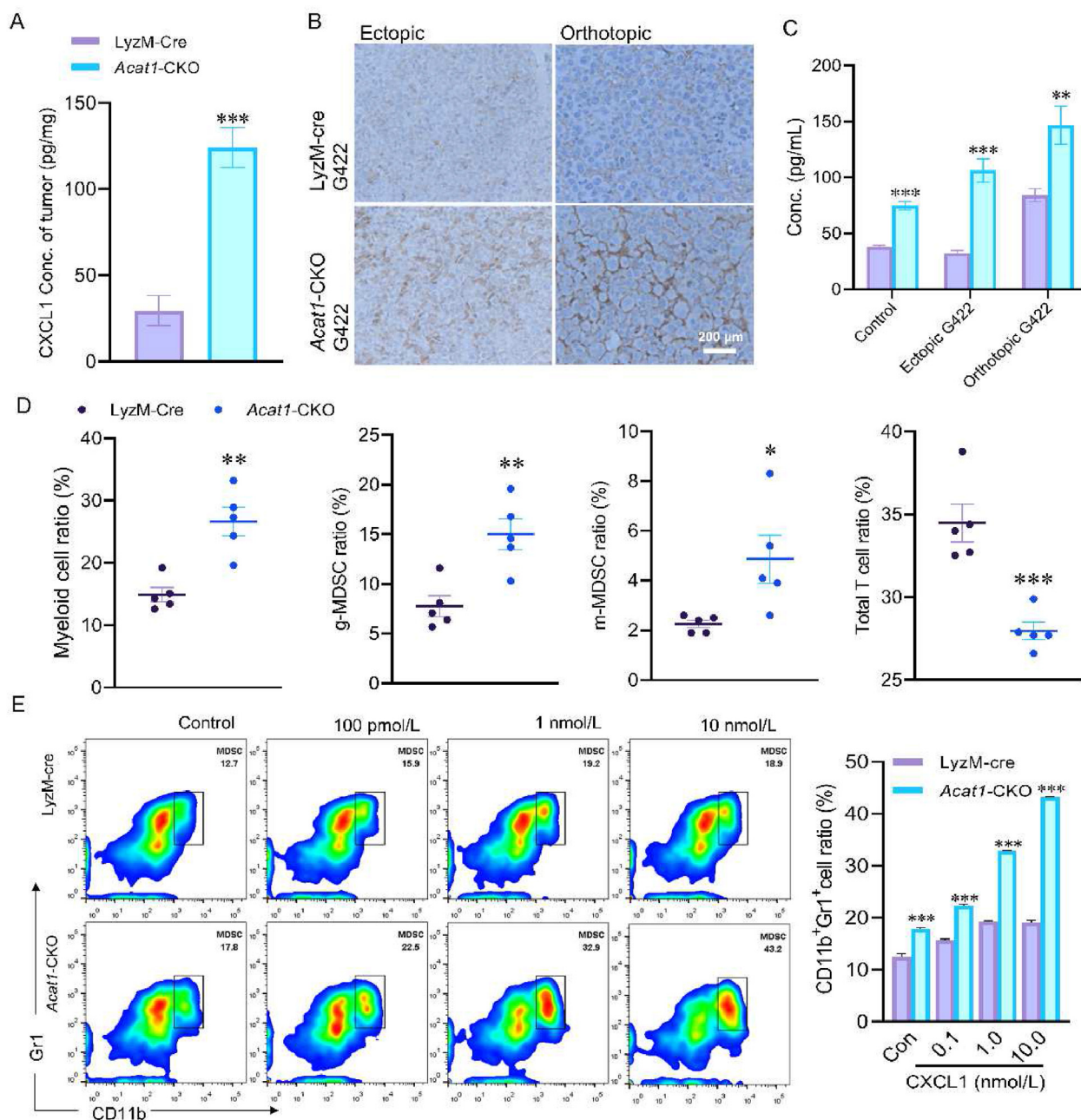


Figure 5 CXCL1 is a key factor to promote MDSCs accumulation after ACAT1 depletion. (A) The protein levels of mouse CXCL1 in ectopic G422 tumors of LyzM-cre ($n = 8$) and *Acat1*-CKO ($n = 8$) mice at 14 days post-tumor cell inoculation. *** $P = 0.000014$. (B) Representative images of CXCL1-stained tumor sections (four images per mouse) of LyzM-cre and *Acat1*-CKO mice. (C) Serum CXCL1 level of tumor-free ($n = 3$) mice and mice with ectopic ($n = 8$) or orthotopic ($n = 5$) G422 glioma model as described in Fig. 2. *** $P = 0.00076$, *** $P = 7.4E-6$, ** $P = 0.0080$. (D) The indicated leukocyte ratio in the blood of normal LyzM-cre ($n = 5$) and *Acat1*-CKO ($n = 5$) mice without treatment. ** $P = 0.00172$, ** $P = 0.00469$, * $P = 0.0282$, *** $P = 0.000832$. (E) Flow cytometry analysis (left) and percentage (right) of MDSCs (CD11b⁺/Gr1⁺) in the bone marrow cells cultured in complete RPMI medium containing GM-CSF and IL-6 from LyzM-cre ($n = 3$) and *Acat1*-CKO ($n = 3$) mice on the fourth day induced by CXCL1 of indicated concentration. *** $P = 0.00097$, *** $P = 1.85E-5$, *** $P = 3.67E-7$, *** $P = 9.53E-7$.

proliferation (Fig. 3G). Targeting MDSCs and identifying specific molecules that mediate MDSC development will not only facilitate the R&D of novel drugs but also improve currently available therapies.

Growing pieces of evidence demonstrated that enzymes involved in FAO play a pivotal role in the regulation of the function of immune cells^{57,58}. ACAT1, an enzyme primarily

located in the mitochondria, catalyzes the reversible conversion of acetoacetyl-CoA into two acetyl-CoA molecules. In addition to its role in energy metabolism, ACAT1 also possesses acetyltransferase activity^{22–25}. Currently, there are no clinical applications of ACAT1-targeted drugs. However, Fan et al. identified a partial agonist of nicotinic and muscarinic acetylcholine receptor, arecoline hydrobromide, as a covalent ACAT1 inhibitor that

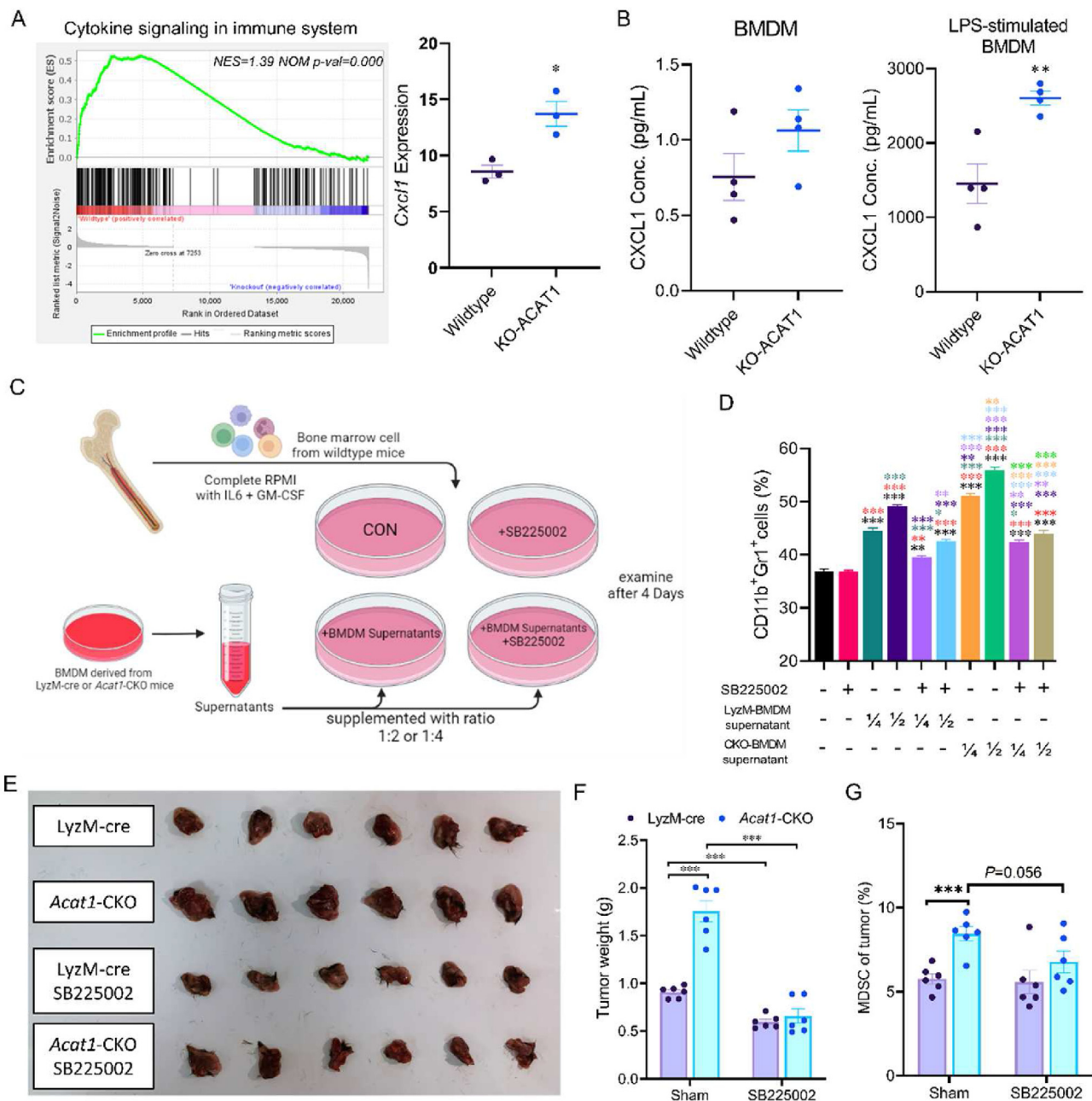


Figure 6 More CXCL1 derived from ACAT1-knockout M ϕ promoted MDSCs accumulation. (A) GSEA plot (left) and *Cxcl1* expression (right) of the RNA-seq data of bone marrow-derived wt and *Acat1*^{-/-} M ϕ . NES, normalized enrichment score. $n = 3$ mice per group. Statistical significance was determined by linear modeling and Bayesian statistics after correcting for multiple testing using the Wald test with Benjamini–Hochberg’s multiple-comparison correction. * $P = 0.015$. (B) The protein levels of CXCL1 in the cell culture supernatants of resting (left) and 100 ng/mL LPS-stimulated (right) BMDMs for 24 h. $n = 4$ culture per group. ** $P = 0.0063$. (C) Bone marrow cells were cultured with 2 μ mol/L SB225002 or a different ratio of BMDM culture supernatant cultured for 24 h derived from the *LyzM-cre* and *Acat1*-CKO mice as depicted. (D) Percentage of CD11b⁺GR1⁺ cells in the bone marrow cells measured by flow cytometry. $n = 3$ culture per group. “*” represents the result of the t -test analysis with the corresponding color bar, * $P < 0.05$, ** $P < 0.01$, *** $P < 0.001$. (E, F) Tumor image (E) and tumor weight (F) in G422-burden *LyzM-cre* and *Acat1*-CKO mice treated with 10 mg/kg SB225002 by i.p. injection every day ($n = 6$ mice per group), mice were sacrificed after the 14th day. *** $P < 0.001$. (G) Percentage of MDSCs in ectopic G422 tumors of *LyzM-cre* ($n = 6$) and *Acat1*-CKO ($n = 6$) mice injected SB225002, as determined by flow cytometry. *** $P < 0.001$.

specifically binds to and disrupts ACAT1 tetramers^{25,59}. The limited availability of tool compounds has posed significant challenges in the development of therapeutics targeting ACAT1. Our study indicated that myeloid ACAT1 could regulate MDSC

development and represents a promising target for tumor immunotherapy. Moreover, ACAT1 plays a critical role in oxidative phosphorylation, phagocytic capacity, and antigen presentation function of M ϕ . The alteration of M ϕ in the cytokine secretion

profile is associated with changes in cellular oxidative phosphorylation status (Fig. S6). However, the specific mechanism by which ACAT1 exerts its regulatory role, such as controlling protein acetylation modifications or influencing cellular metabolism, requires further investigation. ACAT1's critical involvement in myeloid cell differentiation suggests its potential as a therapeutic target for treating glioblastoma characterized by elevated levels of myeloid cells in tumor tissue or blood.

Chemokines, a class of molecules, have been recognized for their ability to regulate the motility of leukocytes into tissues⁶⁰. According to increasing body evidence, chemokines are required for tumor progression, metastasis, angiogenesis, hematopoiesis, and therapeutic resistance in cancer⁶⁰. CXCL1, belonging to the chemotactic superfamily, is highly expressed in several cancer types, including melanoma⁶¹, colorectal cancer⁴⁶, breast cancer⁴⁸, and glioblastoma⁶². Studies have shown that CXCL1 not only promotes tumor progression independently but also attracts neutrophils and MDSCs expressing CXCR2 from the circulation toward tumor tissues to form an immunosuppressive TME^{46,63}. CXCL1 has been identified as one of the most secreted cytokines from tumor-associated M ϕ , and we observed an increase in M ϕ -secreted CXCL1 increased following ACAT1 depletion in myeloid cells (Fig. 5A–C). The phenomenon is consistent with the elevated MDSCs level in blood and tumor tissue of *Acat1*-CKO mice. The administration of SB225002, a CXCL1 pathway inhibitor, effectively suppresses tumor growth in CKO mice through down-regulating MDSC level (Fig. 6E–G), which hints that CXCL1 was a vital promoter of MDSCs accumulation. Lefler et al.⁶⁴ reported that increased phosphorylation of STAT3 Tyr705 promotes the secretion of CXCL1. In our research, we observed an elevation in STAT3 Tyr705 phosphorylation in peritoneal M ϕ s and BMDMs upon ACAT1 deficiency (Fig. S5G). This finding suggests a potential association between the increased phosphorylation of STAT3 Tyr705 and the elevated levels of CXCL1 secretion. However, the precise mechanism that how ACAT1 influenced CXCL1 production by M ϕ is still being investigated in our ongoing studies, and the potential of CXCL1 as a prognostic biomarker and effective therapeutic target in patients with glioblastoma still requires further validation through additional clinical data.

A substantial of GBM patients who do not respond to conventional treatments, especially immunotherapy, often present a notable infiltration of MDSC-dominated myeloid cells^{65,66}. Consistent with these observations, our study also revealed a significant decrease in T cells accompanied by increased infiltration of MDSCs. Thus, targeting myeloid cells may hold promise for enhancing the efficacy of cancer immunotherapy in GBM. However, the TME is highly complex, consisting not only of tumor cells but also a significant infiltration of immune cells. In this study, we specifically investigated the critical role of myeloid-ACAT1 in promoting tumor progression through the accumulation of MDSCs. However, the functional impact of ACAT1 on other cell types within the TME remains largely unexplored, posing challenges in the development of this target. Furthermore, although we observed a relationship between ACAT1 expression and tumor myeloid cells in patient tumor tissues, using ACAT1 expression in tumors as a means to assess tumor progression still lacks supporting data. In addition, the myeloid checkpoint has also been postulated by researchers²⁸, which serves as a crucial supplement to the immune checkpoint. However, there were still several questions that remained to be addressed such as if there were any other important myeloid checkpoints and the mechanisms through which these checkpoints regulate anti-tumor responses.

Based on the aforementioned studies, it is evident that ACAT1 plays a pivotal role in myeloid cell biology. Deletion of ACAT1 leads to an increased proportion of myeloid cells, particularly MDSCs, within tumors and in the bloodstream. Consequently, this alteration promotes the formation of an immunosuppressive microenvironment conducive to tumor growth, characterized by the reduced number of effector T cells in the tumor tissue. The significance of ACAT1 in myeloid cell development and function highlights its potential as an intriguing and promising drug target.

5. Conclusions

Our findings demonstrate that the deletion of ACAT1 in myeloid cells leads to the accumulation of MDSCs in tumor-bearing mice and is crucial for maintaining myeloid cell homeostasis. ACAT1 not only influences myeloid cell differentiation, resulting in the accumulation of MDSCs, but also ACAT1-deficient M ϕ s secrete more CXCL1 which motivates the formation and accumulation of MDSCs, contributing to the development of an immunosuppressive microenvironment and ultimately facilitating tumor progression.

Acknowledgments

We acknowledge the assistance of Chinese Academy of Medical Sciences & Peking Union Medical College and the Institute of Materia Medica. This study was supported by National Key R&D Program of China (No. 2019YFE0111800), National Natural Science Foundation of China (Nos. T2192972, 81872923, and 81903904), and the CAMS Innovation Fund (2022-I2M-1-014, China).

Author contributions

Mingjin Wang: Conceptualization, Methodology, Writing-Original Draft. Weida Wang: Methodology, Resources, Investigation. Shen You: Formal analysis, Data Curation. Zhenyan Hou: Validation, Software. Tingting Du, Nina Xue, and Ming Ji: Supervision, Investigation. Xiaoguang Chen: Conceptualization, Supervision, Funding acquisition. Jing Jin: Writing-Review & Editing, Project administration.

Conflicts of interest

The authors declare no conflicts of interest.

Appendix A. Supporting information

Supporting data to this article can be found online at <https://doi.org/10.1016/j.apsb.2023.09.005>.

References

1. De Leo A, Ugolini A, Veglia F. Myeloid cells in glioblastoma microenvironment. *Cells* 2020;**10**:18.
2. Cancer Genome Atlas Research Network, Brat DJ, Verhaak RG, Aldape KD, Yung WK, Salama SR, Cooper LA, et al. Comprehensive, integrative genomic analysis of diffuse lower-grade gliomas. *N Engl J Med* 2015;**372**:2481–98.
3. McKinnon C, Nandhabalan M, Murray SA, Plaha P. Glioblastoma: clinical presentation, diagnosis, and management. *BMJ* 2021;**374**:n1560.

4. Stupp R, Taillibert S, Kanner A, Read W, Steinberg DM, Lhermitte B, et al. Effect of tumor-treating fields plus maintenance temozolomide vs maintenance temozolomide alone on survival in patients with glioblastoma: a randomized clinical trial. *JAMA* 2017;**318**:2306–16.
5. Liu H, Qiu W, Sun T, Wang L, Du C, Hu Y, et al. Therapeutic strategies of glioblastoma (GBM): the current advances in the molecular targets and bioactive small molecule compounds. *Acta Pharm Sin B* 2022;**12**:1781–804.
6. Pinton L, Magri S, Masetto E, Vettore M, Schibuola I, Ingangi V, et al. Targeting of immunosuppressive myeloid cells from glioblastoma patients by modulation of size and surface charge of lipid nanoparticles. *J Nanobiotechnol* 2020;**18**:31.
7. Yang Q, Guo N, Zhou Y, Chen J, Wei Q, Han M. The role of tumor-associated macrophages (TAMs) in tumor progression and relevant advance in targeted therapy. *Acta Pharm Sin B* 2020;**10**:2156–70.
8. Liu X, Yin M, Dong J, Mao G, Min W, Kuang Z, et al. Tubeimoside-1 induces TFEB-dependent lysosomal degradation of PD-L1 and promotes antitumor immunity by targeting mTOR. *Acta Pharm Sin B* 2021;**11**:3134–49.
9. Stromnes IM, Brockenbrough JS, Izeradjene K, Carlson MA, Cuevas C, Simmons RM, et al. Targeted depletion of an MDSC subset unmasks pancreatic ductal adenocarcinoma to adaptive immunity. *Gut* 2014;**63**:1769–81.
10. Zhou J, Nefedova Y, Lei A, Gabrilovich D. Neutrophils and PMN-MDSC: their biological role and interaction with stromal cells. *Semin Immunol* 2018;**35**:19–28.
11. Steinberg SM, Shabaneh TB, Zhang P, Martyanov V, Li Z, Malik BT, et al. Myeloid cells that impair immunotherapy are restored in melanomas with acquired resistance to BRAF inhibitors. *Cancer Res* 2017;**77**:1599–610.
12. Snaebjornsson MT, Janaki-Raman S, Schulze A. Greasing the wheels of the cancer machine: the role of lipid metabolism in cancer. *Cell Metabol* 2020;**31**:62–76.
13. Li W, Cai H, Ren L, Yang Y, Yang H, Liu J, et al. Sphingosine kinase 1 promotes growth of glioblastoma by increasing inflammation mediated by the NF- κ B/IL-6/STAT3 and JNK/PTX3 pathways. *Acta Pharm Sin B* 2022;**12**:4390–406.
14. Kou Y, Geng F, Guo D. Lipid metabolism in glioblastoma: from *de novo* synthesis to storage. *Biomedicines* 2022;**10**:1943.
15. Lee H, Kim D, Youn B. Targeting oncogenic rewiring of lipid metabolism for glioblastoma treatment. *Int J Mol Sci* 2022;**23**:13818.
16. Li X, Li Y, Yu Q, Qian P, Huang H, Lin Y. Metabolic reprogramming of myeloid-derived suppressor cells: an innovative approach confronting challenges. *J Leukoc Biol* 2021;**110**:257–70.
17. Yan D, Yang Q, Shi M, Zhong L, Wu C, Meng T, et al. Polyunsaturated fatty acids promote the expansion of myeloid-derived suppressor cells by activating the JAK/STAT3 pathway. *Eur J Immunol* 2013;**43**:2943–55.
18. Yan D, Adeshakin AO, Xu M, Afolabi LO, Zhang G, Chen YH, et al. Lipid metabolic pathways confer the immunosuppressive function of myeloid-derived suppressor cells in tumor. *Front Immunol* 2019;**10**:1399.
19. Won WJ, Dshane JS, Leavenworth JW, Oliva CR, Griguer CE. Metabolic and functional reprogramming of myeloid-derived suppressor cells and their therapeutic control in glioblastoma. *Cell Stress* 2019;**3**:47–65.
20. Hu C, Pang B, Lin G, Zhen Y, Yi H. Energy metabolism manipulates the fate and function of tumour myeloid-derived suppressor cells. *Br J Cancer* 2020;**122**:23–9.
21. Tiwari SK, Toshniwal AG, Mandal S, Mandal L. Fatty acid β -oxidation is required for the differentiation of larval hematopoietic progenitors in *Drosophila*. *Elife* 2020;**9**:e53247.
22. Zhou P, Zhu Z, Hidayatullah Khan M, Zheng P, Teng M, Niu L. Crystal structure of cytoplasmic acetoacetyl-CoA thiolase from *Saccharomyces cerevisiae*. *Acta Crystallogr F Struct Biol Commun* 2018;**74**:6–13.
23. Goudarzi A. The recent insights into the function of ACAT1: a possible anti-cancer therapeutic target. *Life Sci* 2019;**232**:116592.
24. Chen D, Xia S, Zhang R, Li Y, Famulare CA, Fan H, et al. Lysine acetylation restricts mutant IDH2 activity to optimize transformation in AML cells. *Mol Cell* 2021;**81**:3833–3847.e11.
25. Fan J, Lin R, Xia S, Chen D, Elf SE, Liu S, et al. Tetrameric acetyl-CoA acetyltransferase 1 is important for tumor growth. *Mol Cell* 2016;**64**:859–74.
26. Zhang L, Li Z, Skrzypczynska KM, Fang Q, Zhang W, O'Brien SA, et al. Single-cell analyses inform mechanisms of myeloid-targeted therapies in colon cancer. *Cell* 2020;**181**:442–459.e29.
27. Xi Q, Wang M, Jia W, Yang M, Hu J, Jin J, et al. Design, synthesis, and biological evaluation of amidobenzimidazole derivatives as stimulator of interferon genes (STING) receptor agonists. *J Med Chem* 2020;**63**:260–82.
28. Li T, Li X, Zamani A, Wang W, Lee CN, Li M, et al. c-Rel is a myeloid checkpoint for cancer immunotherapy. *Nat Can (Ott)* 2020;**1**:507–17.
29. Ip WKE, Hoshi N, Shouval DS, Snapper S, Medzhitov R. Anti-inflammatory effect of IL-10 mediated by metabolic reprogramming of macrophages. *Science* 2017;**356**:513–9.
30. Zhao W, Dovas A, Spinazzi EF, Levitin HM, Banu MA, Upadhyayula P, et al. Deconvolution of cell type-specific drug responses in human tumor tissue with single-cell RNA-seq. *Genome Med* 2021;**13**:82.
31. Yuan J, Levitin HM, Frattini V, Bush EC, Boyett DM, Samanamud J, et al. Single-cell transcriptome analysis of lineage diversity in high-grade glioma. *Genome Med* 2018;**10**:57.
32. Wang L, Babikir H, Müller S, Yagnik G, Shamardani K, Catalan F, et al. The phenotypes of proliferating glioblastoma cells reside on a single axis of variation. *Cancer Discov* 2019;**9**:1708–19.
33. Park JH, Feroze AH, Emerson SN, Mihalas AB, Keene CD, Cimino PJ, et al. A single-cell based precision medicine approach using glioblastoma patient-specific models. *npj Precis Oncol* 2022;**6**:55.
34. Niikura N, Iwamoto T, Masuda S, Kumaki N, Xiaoyan T, Shirane M, et al. Immunohistochemical Ki67 labeling index has similar proliferation predictive power to various gene signatures in breast cancer. *Cancer Sci* 2012;**103**:1508–12.
35. Xu J, Fang J, Cheng Z, Fan L, Hu W, Zhou F, et al. Overexpression of the Kininogen-1 inhibits proliferation and induces apoptosis of glioma cells. *J Exp Clin Cancer Res* 2018;**37**:180.
36. Grzywa TM, Sosnowska A, Matryba P, Rydzynska Z, Jasinski M, Nowis D, et al. Myeloid cell-derived arginase in cancer immune response. *Front Immunol* 2020;**11**:938.
37. Steggerda SM, Bennett MK, Chen J, Emberley E, Huang T, Janes JR, et al. Inhibition of arginase by CB-1158 blocks myeloid cell-mediated immune suppression in the tumor microenvironment. *J Immunother Cancer* 2017;**5**:101.
38. Maimon A, Levi-Yahid V, Ben-Meir K, Halpern A, Talmi Z, Priya S, et al. Myeloid cell-derived PROS1 inhibits tumor metastasis by regulating inflammatory and immune responses via IL-10. *J Clin Invest* 2021;**131**:e126089.
39. Guo X, Qiu W, Liu Q, Qian M, Wang S, Zhang Z, et al. Immunosuppressive effects of hypoxia-induced glioma exosomes through myeloid-derived suppressor cells via the miR-10a/Rora and miR-21/Pten Pathways. *Oncogene* 2018;**37**:4239–59.
40. Propper DJ, Balkwill FR. Harnessing cytokines and chemokines for cancer therapy. *Nat Rev Clin Oncol* 2022;**19**:237–53.
41. Alshetaiwi H, Pervolarakis N, McIntyre LL, Ma D, Nguyen Q, Rath JA, et al. Defining the emergence of myeloid-derived suppressor cells in breast cancer using single-cell transcriptomics. *Sci Immunol* 2020;**5**:e6017.
42. Nakamura K, Smyth MJ. Myeloid immunosuppression and immune checkpoints in the tumor microenvironment. *Cell Mol Immunol* 2020;**17**:1–12.
43. Condamine T, Gabrilovich DI. Molecular mechanisms regulating myeloid-derived suppressor cell differentiation and function. *Trends Immunol* 2011;**32**:19–25.
44. Lechner MG, Liebertz DJ, Epstein AL. Characterization of cytokine-induced myeloid-derived suppressor cells from normal

- human peripheral blood mononuclear cells. *J Immunol* 2010;**185**:2273–84.
45. Groth C, Hu X, Weber R, Fleming V, Altevogt P, Utikal J, et al. Immunosuppression mediated by myeloid-derived suppressor cells (MDSCs) during tumour progression. *Br J Cancer* 2019;**120**:16–25.
 46. Wang D, Sun H, Wei J, Cen B, DuBois RN. CXCL1 is critical for premetastatic niche formation and metastasis in colorectal cancer. *Cancer Res* 2017;**77**:3655–65.
 47. Kumar V, Patel S, Tcyganov E, Gabrilovich DI. The nature of myeloid-derived suppressor cells in the tumor microenvironment. *Trends Immunol* 2016;**37**:208–20.
 48. Wang N, Liu W, Zheng Y, Wang S, Yang B, Li M, et al. CXCL1 derived from tumor-associated macrophages promotes breast cancer metastasis via activating NF- κ B/SOX4 signaling. *Cell Death Dis* 2018;**9**:880.
 49. Ryan DG, Murphy MP, Frezza C, Prag HA, Chouchani ET, O'Neill LA, et al. Coupling Krebs cycle metabolites to signalling in immunity and cancer. *Nat Metab* 2019;**1**:16–33.
 50. Weiskopf K, Weissman IL. Macrophages are critical effectors of antibody therapies for cancer. *mAbs* 2015;**7**:303–10.
 51. Guerriero JL. Macrophages: their untold story in T cell activation and function. *Int Rev Cell Mol Biol* 2019;**342**:73–93.
 52. Yeo AT, Rawal S, Delcuze B, Christofides A, Atayde A, Strauss L, et al. Single-cell RNA sequencing reveals evolution of immune landscape during glioblastoma progression. *Nat Immunol* 2022;**23**:971–84.
 53. Klemm F, Maas RR, Bowman RL, Kornete M, Soukup K, Nassiri S, et al. Interrogation of the microenvironmental landscape in brain tumors reveals disease-specific alterations of immune cells. *Cell* 2020;**181**:1643–1660.e17.
 54. Mi Y, Guo N, Luan J, Cheng J, Hu Z, Jiang P, et al. The emerging role of myeloid-derived suppressor cells in the glioma immune suppressive microenvironment. *Front Immunol* 2020;**11**:737.
 55. Veglia F, Perego M, Gabrilovich D. Myeloid-derived suppressor cells coming of age. *Nat Immunol* 2018;**19**:108–19.
 56. Raber P, Ochoa AC, Rodríguez PC. Metabolism of L-arginine by myeloid-derived suppressor cells in cancer: mechanisms of T cell suppression and therapeutic perspectives. *Immunol Invest* 2012;**41**:614–34.
 57. Ma Y, Temkin SM, Hawkrigde AM, Guo C, Wang W, Wang XY, et al. Fatty acid oxidation: an emerging facet of metabolic transformation in cancer. *Cancer Lett* 2018;**435**:92–100.
 58. Zheng M, Zhang W, Chen X, Guo H, Wu H, Xu Y, et al. The impact of lipids on the cancer-immunity cycle and strategies for modulating lipid metabolism to improve cancer immunotherapy. *Acta Pharm Sin B* 2023;**13**:1488–97.
 59. Liu YJ, Peng W, Hu MB, Xu M, Wu CJ. The pharmacology, toxicology and potential applications of arecoline: a review. *Pharm Biol* 2016;**54**:2753–60.
 60. Acharyya S, Oskarsson T, Vanharanta S, Malladi S, Kim J, Morris PG, et al. A CXCL1 paracrine network links cancer chemoresistance and metastasis. *Cell* 2012;**150**:165–78.
 61. Dhawan P, Richmond A. Role of CXCL1 in tumorigenesis of melanoma. *J Leukoc Biol* 2002;**72**:9–18.
 62. Alafate W, Li X, Zuo J, Zhang H, Xiang J, Wu W, et al. Elevation of CXCL1 indicates poor prognosis and radioresistance by inducing mesenchymal transition in glioblastoma. *CNS Neurosci Ther* 2020;**26**:475–85.
 63. Katoh H, Wang D, Daikoku T, Sun H, Dey SK, Dubois RN. CXCR2-expressing myeloid-derived suppressor cells are essential to promote colitis-associated tumorigenesis. *Cancer Cell* 2013;**24**:631–44.
 64. Lefler JE, MarElia-Bennett CB, Thies KA, Hildreth 3rd BE, Sharma SM, Pitarresi JR, et al. STAT3 in tumor fibroblasts promotes an immunosuppressive microenvironment in pancreatic cancer. *Life Sci Alliance* 2022;**5**:e202201460.
 65. Pearson JRD, Cuzzubbo S, McArthur S, Durrant LG, Adhikaree J, Tinsley CJ, et al. Immune escape in glioblastoma multiforme and the adaptation of immunotherapies for treatment. *Front Immunol* 2020;**11**:582106.
 66. De Cicco P, Ercolano G, Ianaro A. The new era of cancer immunotherapy: targeting myeloid-derived suppressor cells to overcome immune evasion. *Front Immunol* 2020;**11**:1680.